Turbulent Heating in the Accelerating Region Using a Multishell Model

Solar Physics
DOI: 10.1007/•••••-•••-•••-••••-•

Turbulent heating in the accelerating region using a multishell model

Andrea Verdini[1] · Roland Grappin[2] · Victor Montagud-Camps[2]

Abstract Recent studies of turbulence driven solar winds indicate that fast winds are obtained only at the price of unrealistic bottom boundary conditions: too large wave amplitudes and small frequencies. In these works, the incompressible turbulent dissipation is modelled with a large-scale von Karman-Howart-Kolmogorov-like phenomenological expression (Q^0_{K41}). An evaluation of the phenomenology is thus necessary to understand if unrealistic boundary conditions result from physical or model limitations. To assess the validity of the Kolmogorov-like expression, Q^0_{K41}, one needs to compare it to exact heating, which requires describing the cascade in detail. This has been done in the case of homogeneous MHD turbulence, including expansion, but not in the critical accelerating region. To assess the standard incompressible turbulent heating in the accelerating region, we use a reduced MHD model (multishell model) in which the perpendicular turbulent cascade is described by a shell model, allowing to reach a Reynolds number of 10^6. We first consider the homogeneous and expanding cases, and find that primitive MHD and multishell equations give remarkably similar results. We thus feel free to use the multishell model in the accelerating region. The results indicate that the large-scale phenomenology is inaccurate and it overestimates the heating by a factor at least 20, thus invalidating earlier studies of winds driven by incompressible turbulence. We conclude that realistic 1D wind models cannot be based solely on incompressible turbulence, but probably need an addition of compressible turbulence and shocks to increase the wave reflection and thus the heating.

✉ A. V. Verdini
andrea.verdini@unifi.it

R. G. Grappin
roland.grappin@lpp.polytechnique.fr

V. M. Montagud-Camps
victor.montagud-camps@lpp.polytechnique.fr

[1] Dipartimento di Fisica e Astronomia, Universitá di Firenze

[2] Laboratoire de Physique des Plasmas, École Polytechnique

Keywords: Coronal Holes, Solar Wind, Theory, Turbulence, Magnetohydrodynamics

1. Introduction

Solar wind models with assigned heating profiles, $Q(R)$, (Wang, 1994) vs heliocentric distance, R, allowed us to understand how the amount and profile of heating, together with the magnetic tube section $A(R)$, control the wind properties (Wang *et al.*, 2012)). As a further step one needs to find suitable processes that are able to produce adequate heating profiles: this remains today an important issue of solar wind physics.

We focus on one-dimensional, fluid, solar-wind models that are driven either by incompressible-turbulent or by compressible dissipation. By solar-wind models we refer to models that rely on self-consistent heating mechanisms to obtain the bulk velocity, density, and temperature of the wind. The incompressible turbulent model is partly phenomenological (e.g. Cranmer, van Ballegooijen, and Edgar, 2007; Verdini *et al.*, 2010; Chandran *et al.*, 2011; Lionello *et al.*, 2014; Woolsey and Cranmer, 2015). It describes exactly the wave propagation along the average magnetic field line (coinciding with the radial direction). Heating is due to a perpendicular turbulent cascade that is not described: only its final result, the turbulent dissipation, is represented by a phenomenological expression, Q^0_{K41}, to be defined below in Equation 1 (Dmitruk, Milano, and Matthaeus, 2001), which is a generalization to MHD of the von Karman-Howart expression (Hossain *et al.*, 1995). Conversely, the compressible model (Suzuki and Inutsuka, 2005) completely neglects the perpendicular cascade but describes exactly the radial propagation of all MHD waves (with radial wave vectors) as well as their nonlinear couplings. Heating comes from shock dissipation and no phenomenology is employed since 1D compressible MHD equations are solved directly.

Comparing the two models is instructive. The incompressible model is physically satisfying, since a signature of the incompressible cascade is observed in the far solar wind ($R \geq 0.3$ AU), i.e. a Kolmogorov-like scaling of the turbulent energy spectrum (see review by Bruno and Carbone, 2013). However, the most recent calculations (e.g. Lionello *et al.*, 2014) obtain a fast wind at the price of injecting excessively large turbulent amplitudes at the solar surface (~ 10 km s^{-1}) with zero frequency, that is unrealistic and maximizes the heating (e.g. Verdini and Velli, 2007). Conversely, the compressible model achieves fast or slow winds with moderate amplitudes at the surface ($\lesssim 1$ km s^{-1}), and an acceptable frequency spectrum (Suzuki and Inutsuka, 2005; Suzuki and Inutsuka, 2006).

One might thus conclude that the compressible model is by far the best one. However, most available published works, including 3D modeling of the solar wind (e.g. Usmanov, Goldstein, and Matthaeus, 2014; van der Holst *et al.*, 2014), deal with the incompressible model, probably for two reasons: (i) the compressible model requires more than an order of magnitude greater number of mesh points than the incompressible model, making it computationally demanding

to extend to higher dimensions (but see Matsumoto and Suzuki, 2012, for a 2D version); (ii) as already mentioned the only turbulent signature directly observed in the Heliosphere is that of an incompressible cascade.

The recent paper by Shoda, Yokoyama, and Suzuki (2018) merges the two models by adding the same phenomenological incompressible turbulent damping, Q^0_{K41}, to the 1D compressible MHD model by Suzuki and Inutsuka (2005). One thus has the two heating sources. With reasonable parameters (as surface eddy size of 10 Mm), the source of coronal heating is found to be mainly incompressible and to be large enough to generate a realistic wind, unlike purely incompressible models. We will come back to this result in the discussion.

It is thus fundamental to determine the robustness of the incompressible model, that is, to asses the validity of the phenomenological turbulent heating. Its expression has been tested numerically in the framework of homogeneous MHD turbulence (e.g. Hossain *et al.*, 1995), and recently in the case of the expanding wind in the heliosphere (Montagud-Camps, Grappin, and Verdini, 2018), but not in the accelerating region. For such a test, one should follow the incompressible cascade in a highly stratified atmosphere using direct simulations, which is almost impossible with available computational power (the most promising way is an extension to 3D of the Accelerating Box Model of Tenerani and Velli 2017). Indeed, several authors carried out Reduced MHD simulations of turbulence in a stratified corona (Dmitruk *et al.*, 2002), also including an accelerating wind (Perez and Chandran, 2013; van Ballegooijen and Asgari-Targhi, 2016, 2017), by employing at best 128 perpendicular modes. At such resolutions, the heating rate varies with the Reynolds number and no reasonable assessment of the phenomenological expression can be made. This is possibly at the source of differing reported results: Dmitruk *et al.* (2002) found that the phenomenology is about a factor 2 larger than the actual heating, while van Ballegooijen and Asgari-Targhi (2016, 2017) found a factor about 20.

We thus propose in the present work to evaluate the heating expression by using an intermediary model, the multishell (or Reduced MHD shell model), which allows to describe the perpendicular turbulent cascade at Reynolds numbers of order 10^6, at the price of a strong decimation of the triadic coupling terms. We shall compare the phenomenological von Karman-Howart expression, Q^0_{K41}, to the exact heating rate obtained by the multishell model in the three cases: turbulence in an homogeneous domain, in an expanding wind with constant speed, and in the acceleration region.

The plan is as follows. In section 2, we give our definitions and method, the exact and approximate expressions allowing to measure the turbulent heating, and we briefly describe the numerical turbulence model (multishell) which we will use for our simulations. In section 3, we give the simulation results for the case of homogeneous turbulent flows with vanishing cross helicity, and of expanding flows with vanishing or maximal cross-helicity (zero or maximal imbalance between the two Alfvén species). In each case, we consider three values of the turbulence strength parameter, ranging from strong to weak turbulent regimes, as measured by the ratio between linear Alfvén time to nonlinear time. The cases with vanishing cross helicity (homogeneous and expanding) are compared to earlier results already obtained with direct MHD numerical simulations. In

section 4, we give the simulation results for the case of turbulent evolution in a coronal hole, varying successively one of the three parameters that characterize the waves injected at the surface: amplitude, correlation length, and correlation time.

2. Basic physics and method

2.1. Measuring turbulent heating in incompressible turbulence: approximate and exact measurements

There are several ways to estimate the turbulent heating, depending on whether the model contains a description of the turbulent cascade or not. In the former case, exact or good estimates can be obtained; in the latter case, the only available measurements deal with the largest eddies, which may give a result far from reality. We give below the different definitions.

2.1.1. Large scale estimate

Solar wind incompressible models are devoid of any description of the turbulent cascade[1]. The turbulent energy decay, and so the turbulent heating, may be obtained only by employing large-scale quantities combined in a generalized von Karman-Howart phenomenological expression (Hossain *et al.*, 1995), with an assigned profile with distance of the eddy containing scale (Dmitruk, Milano, and Matthaeus, 2001),

$$Q^0_{K41} = \frac{1}{2}\frac{|\delta z_-|\delta z_+^2 + |\delta z_+|\delta z_-^2}{2L_\perp}, \tag{1}$$

where $z_\pm = u \pm b$ are the so-called Elsasser variables, with u being the velocity fluctuation, $b = \delta B/\sqrt{4\pi\rho}$, the magnetic field fluctuations in Alfvén units, and with $\delta z_\pm,\ \delta u, \delta b$ indicating the rms values of fluctuations, which is generally dominated by the large scales. $L_\perp = L_\perp(R)$ is the perpendicular correlation scale of the fluctuations; it increases with height, $L_\perp = L_{\perp 0} \times \sqrt{A(R)}$, with A the flux tube section. The base correlation length $L_{\perp 0}$ is chosen to be between the size of the supergranulation (≈ 34 Mm) and that of bright dots (1 Mm).

This expression was originally introduced by Dmitruk, Milano, and Matthaeus (2001) and Dmitruk *et al.* (2002) to study turbulence in static stratified coronae, allowing for a constant parameter, $c_d \approx 1$, on the rhs of Equation 1. For simplicity, we will not use any constant since most authors set $c_d = 1$ in their solar wind models (Cranmer, van Ballegooijen, and Edgar, 2007; Verdini *et al.*, 2010; Chandran *et al.*, 2011; Lionello *et al.*, 2014).

[1]We recall that solar-wind models are those that incorporate incompressible turbulence in a self consistent way, thus excluding studies of incompressible turbulence in a prescribed solar wind profile, as done here.

2.1.2. Inertial range estimate

Another heating estimate consists in evaluating the cascade rate via the amplitude of fluctuations within the inertial range, that is, within the range I in which the 1D energy spectrum follows a $k^{-5/3}$ scaling law, k being the wavenumber. In the hydrodynamic case, the expression reads: $Q_{kol} = ku^3$, in which $k \in I$ and u is the square root of twice the kinetic energy per unit mass included in the waveband $[k/\sqrt{2}, k\sqrt{2}]$. We are interested here in the generalisation to incompressible MHD which reads (Matthaeus *et al.*, 2004):

$$Q_{K41} = \frac{1}{2}k(z_- z_+^2 + z_+ z_-^2). \tag{2}$$

where again $z_\pm$ are evaluated in the waveband $[k/\sqrt{2}, k\sqrt{2}]$ (note that with $\delta z_\pm$ we indicated the rms value of the fluctuations' amplitude, that is, integrated over the spectrum). To be correct, the scale $1/k$ must belong to an inertial range having a power law scaling $k^{-5/3}$: this is a necessary condition if we want the turbulent cascade rate, Q_{K41}, to be scale-independent.

2.1.3. Exact heating

The exact expression for heating in turbulent (or not turbulent) incompressible MHD reads:

$$Q_\nu = \nu\omega^2 + \eta\jmath^2, \tag{3}$$

where ν is the kinematic viscosity, η the resistivity, ω the vorticity and $\jmath$ the current density. Another, equivalent expression will be given in the next section, valid for the reduced MHD (multishell) model that we shall use in this paper.

It is important to remark that measuring the visco-resistive dissipation as done here can be considered as an opening to more general situations. Indeed, let us assume a well-developed turbulence in a quasi-stationary state, and a direct energy cascade from large to small scales. Since the cascade rate is equal to the dissipation rate, measuring the visco-resistive dissipation, Q_ν, is equivalent to measuring the cascade energy flux, e.g. via third-order moments (Politano and Pouquet, 1998; Verdini *et al.*, 2015). Since the cascade rate is independent of the details of the dissipative process, the heating rate should hold also for a plasma in which non-collisional dissipative processes are at work.

2.1.4. Relations between Q^0_{K41}, Q_{K41} and Q_ν

The estimate Q_{K41} usually yields larger values than the actual dissipation because it replaces third-order correlations in the computation of the cascade flux with second order correlations, assuming a $k^{-5/3}$ scaling. The ratio Q_{K41}/Q_ν is a measure of the inefficiency of the cascade: the larger the ratio, the smaller the heating, for a given amplitude of turbulence. A comparison between the phenomenological expression, Q_{K41}, and a close-to-exact estimate of the dissipation, Q_ν, yields $Q_{K41}/Q_\nu \sim 10$ in the slow solar wind at 1 AU (Vasquez *et al.*, 2007).

About the same value was found in 3D compressible MHD simulations of turbulence (Beresnyak, 2012), and also in simulations that included the expansion of the wind (expanding box model) between 0.2 and 1 AU (Montagud-Camps, Grappin, and Verdini, 2018).

A relation between the large-scale Q^0_{K41} and inertial-range Q_{K41} estimates can be found by assuming that the spectra follow a Kolmogorov scaling all the way up to an unknown correlation scale, $L_\perp = 2\pi/k_0$, that is much larger than the scale at which Q_{K41} is evaluated. This allows the rms amplitude to be written as a function of the amplitude in the k_0 band, e.g. $\delta z_+^{rms} \simeq \sqrt{3/2} z_+^0$, and thus to obtain:

$$Q^0_{K41} \simeq Q_{K41} \times (3/2)^{3/2}/4\pi \simeq Q_{K41}/2\pi \tag{4}$$

so that finally

$$\frac{Q^0_{K41}}{Q_\nu} \simeq \frac{1}{2\pi}\frac{Q_{K41}}{Q_\nu} \tag{5}$$

Our aim is to establish whether the large-scale estimate, Q^0_{K41}, is a robust estimate or not of the true heating, Q_ν . We know already that Q_{K41} works quite well at least in the homogeneous and uniformly expanding turbulence, so we shall use Equation 5 to define a proper normalization of Q^0_{K41} before comparing it to Q_ν. However, we shall see that such a relation is not really general, as the inertial range doesn't always reach the largest scales.

2.2. Reduced MHD shell model

To follow the development of turbulence in the acceleration region, we use the multishell model (Verdini, Velli, and Buchlin, 2009), which describes separately the parallel linear dynamics and the perpendicular nonlinear dynamics. First, in the radial direction (parallel to the mean magnetic field), it integrates the primitive MHD equations within a given stratification: density, Alfvén speed, V_A, wind speed, U, and magnetic tube section, $A(R)$, increasing with heliocentric distance, R. Second, the perpendicular nonlinear dynamics at each point of the stratification is integrated via a 2D GOY shell model (Gledzer, 1973; Yamada and Ohkitani, 1987) in the form given by Giuliani and Carbone (1998). Similar models with a uniform density and without a solar wind flow have been used to study the turbulent heating of coronal loops (Nigro *et al.*, 2004; Buchlin and Velli, 2007; Verdini, Grappin, and Velli, 2012). The system integrates the Fourier components $z_\pm(R, k; t)$, with the perpendicular wavenumber k being logarithmically discretized: $k = 2^i k_0$, with $k_0 = k_{00}/(A(R))^{1/2}$, and $i = 0,\ 1,\ ...,\ n_s$, with n_s being the number of shells. Note that the largest perpendicular scale, $1/k_0$, grows with distance as the magnetic tube width, $A(R)^{1/2}$. Nonlinear terms represent approximate nonlinear couplings between nearest-neighbour shells of wavevectors.

In multishell models, dissipation is achieved at small scales by the same terms as in MHD equations, namely (in Fourier space) by visco-resistive terms of the kind

$$\partial_t z_\pm(R, k, t) = ... - \nu k^2 z_\pm(R, k, t), \tag{6}$$

with ν standing for (equal) resistivity and kinematic viscosity. More precisely, the exact dissipation in the multishell system reads at each distance R and time t:

$$\begin{aligned} Q_\nu &= -\partial_t \Sigma_k (1/4)(|z_+(R,k,t)|^2 + |z_-(R,k,t)|^2)|_{visc} \\ &= -(1/2)\Sigma_k \nu k^2 (|z_+|^2 + |z_-|^2). \end{aligned} \tag{7}$$

This expression obtained in the particular case of the multishell system is equivalent to that one given in Equation 3.

The exact heating for the multishell model, Q_ν in Equation 7, will be compared to the phenomenological cascade rate evaluated at an inertial range scale, Q_{K41} as given in Equation 2. The scale is chosen to be the Taylor scale, $1/k_\lambda^\pm$, that is determined independently for each Elsasser field, so as to deal with their unequal amplitudes:

$$Q_{K41}^\lambda = \frac{1}{2}(k_+^\lambda z_- z_+^2 + k_-^\lambda z_+ z_-^2) \tag{8}$$

with:

$$k_\pm^\lambda = (\int k^2 E_\pm(k) dk / \int E_\pm(k) dk)^{1/2}, \tag{9}$$

where $E_\pm(k)$ is the 1D energy spectrum of the Elsasser variables, and the amplitudes $z_\pm$ are computed as the square root of the energies contained in the waveband centred on the Taylor wavenumber,

$$z_\pm = (k_\pm^\lambda E_\pm(k_\pm^\lambda))^{1/2}. \tag{10}$$

In the following we will use the definitions given in Equations 8-10 to analyze our numerical results.

2.2.1. Homogeneous, expanding and coronal hole configurations

We shall use the multishell model in three different versions: (i) homogenous, (ii) expanding, and (iii) coronal hole versions. The numerical domain associated with the expanding and coronal hole versions of the multishell model are sketched in Figure 1, respectively in panels a and b. The mean field direction is along the radial direction, say x.

(i) In the homogeneous version, the density, mean magnetic field, and the magnetic tube section, A, are constant, with periodic boundaries in the x direction (Verdini and Grappin, 2012).

(ii) In the expanding version, we apply the expanding box model (Grappin, Velli, and Mangeney, 1993; Dong, Verdini, and Grappin, 2014) to follow the mean radial wind from 0.2 to 1 AU. The simulation is Lagrangian, that is, we use co-moving coordinates to expand as a transported plasma volume, with again periodic boundary conditions in the mean field direction. During the transport at constant wind speed U_0, the domain covers the distance $R = R_0 + U_0 t$, the flux tube section expands as R^2, and the perpendicular scales increase linearly (so $k_0 \sim 1/R(t)$ in the shell model).

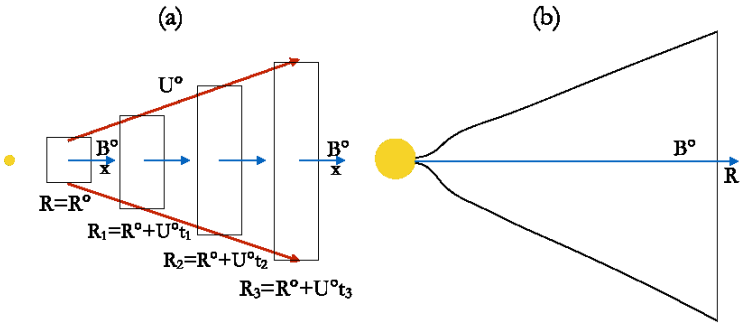

Figure 1. Sketch of the numerical domains (in real space, black contours) considered in the multishell: (a) expanding version; (b) coronal hole. In case (a) the mean wind speed is assumed distance-independant, and the numerical domain (a rectangle) is comoving with the mean wind speed; in case (b) the domain is fixed, and a whole stratification is assumed, see next Figure 2 for details. Note that in both cases the space perpendicular to the radial is actually represented in the multishell by a series logarithmically spaced wavenumbers (see text).

(iii) In the coronal hole version, we use an eulerian absolute frame and follow the evolution from the solar surface up to 10 solar radii. The radial boundaries are transparent to Alfvén waves (open boundaries) (Verdini *et al.*, 2012).

The multishell equations have been used already in the homogeneous and coronal hole cases. In the homogeneous case, they allowed to recover for the first time the double spectral law associated with respectively weak turbulence (k^{-2}) at large scales and strong turbulence ($k^{-5/3}$) at small scales. In the coronal hole version (Verdini and Grappin, 2012), they allowed to show that the low-frequency $1/f$ spectrum was forming naturally in the accelerating region, as a byproduct of the coupled evolution of outward and inward Alfvén waves in this region (Verdini *et al.*, 2012).

2.2.2. Control parameters (homogeneous and expanding cases)

The control parameters will differ depending on the version. In the homogeneous and expanding cases, the parallel/radial boundary conditions are periodic. Due to the absence of boundary conditions, initial conditions completely determine the results. There are three parameters characterizing the initial conditions, which all involve the nonlinear time, $t^0_{NL} = L_\perp/\delta u^{rms}$, with δu^{rms} being the rms amplitude of velocity fluctuations. First, the strength of turbulence, χ, is the ratio of the linear parallel propagation (Alfvén) time, $t^0_A = L_\parallel/B_0$, to the nonlinear time:

$$\chi = \frac{t^0_A}{t^0_{NL}} = \frac{L_\parallel}{L_\perp}\frac{\delta u^{rms}}{B_0}, \tag{11}$$

in which B_0 is the mean magnetic field in Alfvén unit. The second parameter is the expansion parameter which is the non linear time normalized by the linear expansion time:

$$\epsilon_{exp} = \frac{t^0_{NL}}{t^0_{exp}} = \frac{L_\perp}{R_0}\frac{U_0}{\delta u^{rms}}, \tag{12}$$

where U_0 is the (constant) solar wind speed and $R_0 = 0.2AU = L_\perp$ is the initial position of the box for expanding runs ($\epsilon_{exp} \neq 0$). Finally the cross helicity measures the relative amplitudes of the two Aflvén species z_+ and z_-:

$$\sigma_c = \frac{\delta z_+^2 - \delta z_-^2}{\delta z_+^2 + \delta z_-^2}. \tag{13}$$

Its value also can be considered to measure the relative nonlinear times of the two Alfvén species. The parameter values are shown in Table 1.

2.2.3. Boundary conditions (coronal hole version)

In the coronal hole version the boundary conditions are not periodic and the evolution of turbulence with distance depends mainly on the bottom boundary conditions at $R = 1.005\ R_\odot$, while no conditions are imposed at the outer (super-Alfvénic) boundary of the domain. At the bottom boundary we inject incoming Alfvén waves of a given amplitude on three consecutive shells with wavenumbers $k = k_0^{inj} \times [1, 2, 4]$ with $k_0^{inj} = 2\pi/L_{\perp 0}^{inj} = 2^3 k_0$, i.e. we allow for three shells that are larger than injection shells. We thus have three parameters: (i) the amplitude of the injected wave, δz_+^{rms}; (ii) the largest available perpendicular scale, $L_\perp^0 = 1/k_0$; (iii) the correlation time of the injected wave, T^* (the extent of the injected spectrum). A parameter similar to the turbulence strength can be constructed as the ratio of the correlation time and the nonlinear time (for z^-) at the bottom boundary, $\chi_0^- = T^* k_0 \delta z_+^{rms}$.

2.2.4. Spectra and Heating rates

In the following we will systematically show the perpendicular turbulent energy spectra and the exact heating, Q_ν, and compare the latter to the two inertial range and large-scale expressions for the heating. Spectra and heating are functions of time and of the parallel coordinate in the multishell model. We average results in both space and time, but with slightly different intervals.

In homogeneous and expanding runs we are basically interested in the time evolution and we average the heating and the perpendicular spectra along the mean field direction, x. Note that in expanding runs, the plasma volume is a small fraction of the distance range considered (from 0.2 to 1 AU) so the time evolution is directly related to the distance of its center of mass. Spectra are further averaged over one (initial) nonlinear time to increase the statistics.

In coronal runs, we are interested in the spatial distribution of heating and in the spectral evolution with distance. We average the heating and the spectra in time at each position of the grid. For spectra, we further average along a short range in the radial direction (8 consecutive points) to increase statistics.

An example of nonlinear cascade triggered by the reflection of the incident wave in case (iii) is given in Figure 2. The wind model (wind speed, Alfvén speed, density and normalized magnetic tube surface $f = A(R)/(R/R_\odot)^2$) is displayed in the panels (a) and (b). This (fixed) wind model is common to all four runs analyzed later in Section 4. The right panels (c) and (d) show snapshots of the rms

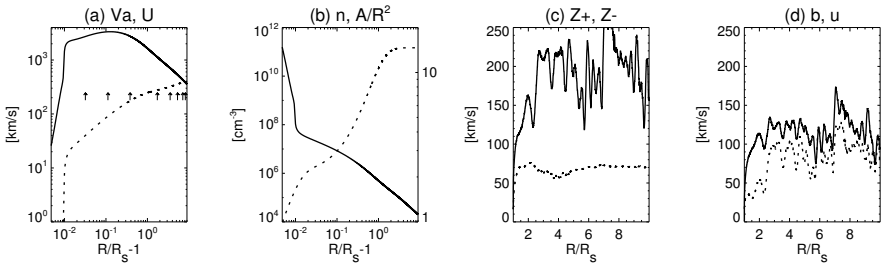

Figure 2. Multishell simulation of turbulence in the accelerating region. (a) and (b): stationary solar wind model, between 1.005 and 10 solar radii (R_s). (a) profiles of the Alfvén speed (*solid line*) and wind speed (*dotted*), the arrows indicate the positions of spectra shown in Figure 5; (b) profiles of density (*solid line*) and over-expansion $f = A(R)/R^2$ (*dotted*). (c) and (d): snapshots of rms amplitudes of fluctuations; (c) z_+ (*solid line*), z_- (*dotted*); (d) magnetic field (*solid line*) and velocity fluctuations (*dotted*).

amplitudes $\delta z_\pm, \delta b, \delta u$, computed by summing the perpendicular energy spectra at each distance R. One sees a large dominance of the incoming component z_+ on the reflected component z_- and a dominance of the magnetic energy on the kinetic energy in the whole corona in the available domain, up to 10 $R_\odot$.

3. Multishell simulations of homogeneous and expanding turbulence

The simulations of homogeneous and expanding turbulence are listed in table 1. The names of runs begin by the letter A, B or C, corresponding to decreasing values of the turbulence strength parameter: $\chi = 5/4,\ 1/2,\ 1/10$. This study will be helpful to interprete the coronal hole configuration in the next Section, in which the turbulence strength parameter is varying with distance. The names of the runs have a suffix: H, E0 and E1, depending on whether it is homogeneous (H), or expanding with no cross-helicity (E0), or expanding with unit cross-helicity (E1). Runs with expansion have $\epsilon_{exp} = 0.4$.

All runs have the following common properties: periodic boundary conditions in the parallel direction, $N_x = 2^{14}$ points in the parallel direction, $n_s = 21$ number of shells for the perpendicular wavenumbers, equal values of viscosity and resistivity at initial time, $\nu_0 = \eta_0 = 8\ 10^{-8}$ (in expanding runs $\nu = \nu_0/R$), and initial rms amplitudes $\delta u^{rms} = \delta b^{rms} = 1$.

The initial condition is obtained by assigning the amplitude and the (random) phase of the Fourier coefficients, $z_\pm(k_\parallel, k)$, inside a maximal wavenumber $k_{max} = 32$ (we recall that k denotes the perpendicular wavenumber, while $k_\parallel$ denotes the parallel one). The amplitudes are chosen to have an initial flat 1D spectrum, $E(k) \sim k^{-1}$. All runs last 10 initial eddy turnover times, corresponding to an increase of distance from 1 to 5 in the expanding case, that is, from 0.2 to 1 AU.

As a final remark, it should be noticed that in *expanding runs* the local measure (not the initial one) of turbulence strength χ is decreasing with distance.

Table 1. Homogeneous and expanding runs with suffix H and $E0$, $E1$ respectively. Initially $\delta u^{rms} = \delta b^{rms} = 1$ in all runs. The parameter χ is the turbulence strength; $L_\parallel$ is the radial (or x) size of the domain; $L^0_\perp = 2\pi$ is the initial transverse size of the domain; B_0 is the initial magnetic field in Alfvén units, ϵ_{exp} is the expansion parameter, and σ_c is the initial cross helicity.

Run	χ	$L_\parallel/L^0_\perp$	B_0	ϵ_{exp}	σ_c
$A_{H,E0,E1}$	5/4	5/2	2	0, 0.4, 0.4	0, 0, 1
$B_{H,E0,E1}$	1/2	1	2	0, 0.4, 0.4	0, 0, 1
$C_{H,E0,E1}$	1/10	1	10	0, 0.4, 0.4	0, 0, 1

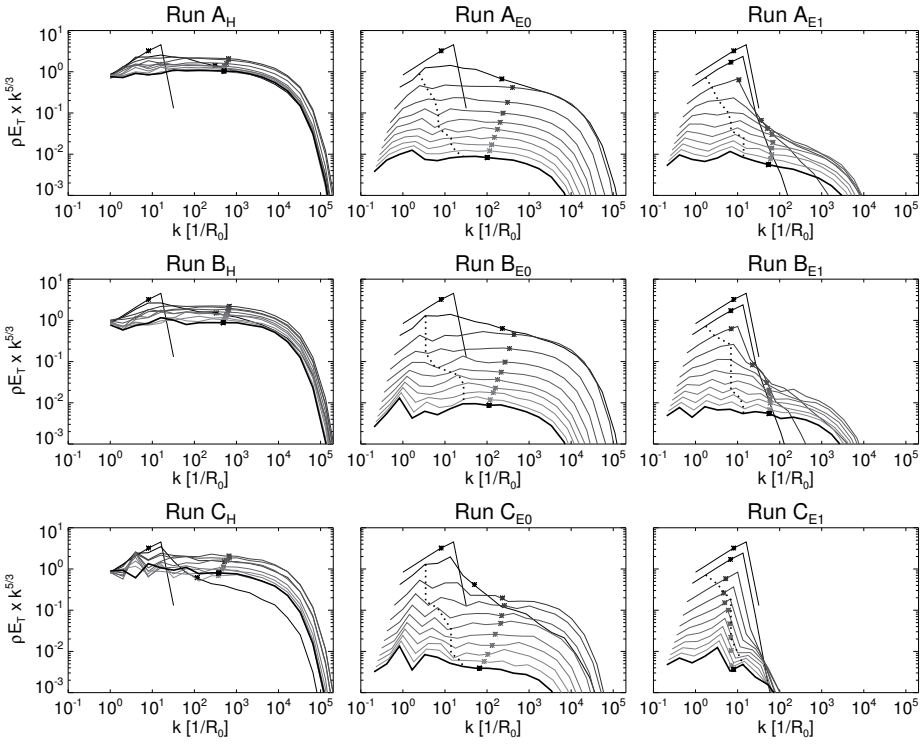

Figure 3. Total energy spectra $\rho E_T(k)$, compensated by $k^{-5/3}$, with k the perpendicular wavenumber, at different times/distances, respectively for homogenous runs (*left column*), expanding runs with $\sigma_c = 0$ (*middle column*), and $\sigma_c = 1$ (*right column*) for the simulations listed in Table 1. From *top* to *bottom*: decreasing turbulence strength. In each panel, symbols indicate the Taylor wavenumber k_λ and the last spectrum is plotted with a *bold line*. In the *middle* and *right columns* the *dotted line* marks the wavenumbers at which $max(t^{\pm}_{NL}) = t_{exp}$. As a rule, the spectra decrease as time/distance increases.

3.1. Spectral evolution

In Figure 3 we plot the evolution with time of the total energy spectra, $\rho E_T = \rho(E_+ + E_-)$, compensated by $k^{-5/3}$ for all the simulations listed in table 1. The density, ρ, is equal to 1 in the homogeneous runs while it decreases as $1/R^2$ in expanding runs (we remind that in expanding runs the distance increases linearly with time, $R/R_0 = 1 + \epsilon_{exp} t$, so as a rule time increases from top to bottom in each panel).

Consider first the group of strong turbulence runs, $A_{H,E0,E1}$ with $\chi = 5/4$, that are plotted in the top row. In the homogenous case (left panel), the energy decreases slowly and the spectra have an extended inertial range with slope $-5/3$ at all times. When introducing expansion (middle panel), the spectra shift to lower k with increasing time due to the stretching of the perpendicular direction, but still maintain a large inertial range with slope $k^{-5/3}$ at all times. Finally, when expansion is combined with an initial maximal cross helicity ($z_- = 0$, right panel), the turbulence cascade is slowed down and the spectra are steeper, possibly having reached an asymptotic slope at late times. In the middle and central panels (expanding runs), the dotted line marks the boundary of equal expansion and nonlinear timescales, with the nonlinear time computed as $t_{NL}(k) = 1/k\delta u_k$. On the right of this line $t_{NL}(k) < t_{exp}$, and the dynamics should be dominated by turbulence. It is in these intervals that power-law spectra develop.

The situation is not very different for intermediate turbulence strength, $\chi = 1/2$, plotted in the middle row (runs $B_{H,E0,E1}$), although the spectra are a bit noisier now. With reference to the central panel (B_{E0}), one can see that the spectra are noisy only at late times, probably because the damping of fluctuations has led to an actual strength that is much smaller than one, but on average they maintain a $-5/3$ slope.

Finally, for the weak turbulence runs, $C_{H,E0,E1}$ with $\chi = 1/10$, the spectra are generally noisy already in the homogenous case (run C_H). The expansion effect is more dramatic, with spectra that are steeper than $k^{-5/3}$ (run C_{E0}), and becomes catastrophic when expansion is combined to the initial maximal cross helicity (run C_{E1}), turbulence is not able to develop at all in this case. Note that in run C_H we do not recover the signature of weak turbulence, a k^{-2} spectrum, that appears instead in the multishell model when a forcing is applied on a large interval of parallel scales (Verdini and Grappin, 2012).

To summarize, in all runs with initial vanishing cross helicity a power-law index close to $-5/3$ is found (the actual value is -1.7), although in expanding runs ($B_{E0},\ C_{E0}$) the spectrum becomes noisy at late times (large distances), possibly because of the decrease of turbulence strength. When the initial cross-helicity is 1, for strong and intermediate turbulence, an inertial range still forms but with a steep slope (runs $A_{E1},\ B_{E1}$). Instead for weak turbulence, a spectrum is not able to develop (run C_{E1}). The Taylor wavenumber, k_λ, is indicated with an asterisk on each spectrum and seems to track quite well the middle of the inertial range, encouraging the use of Q^{λ}_{K41} to estimate the heating.

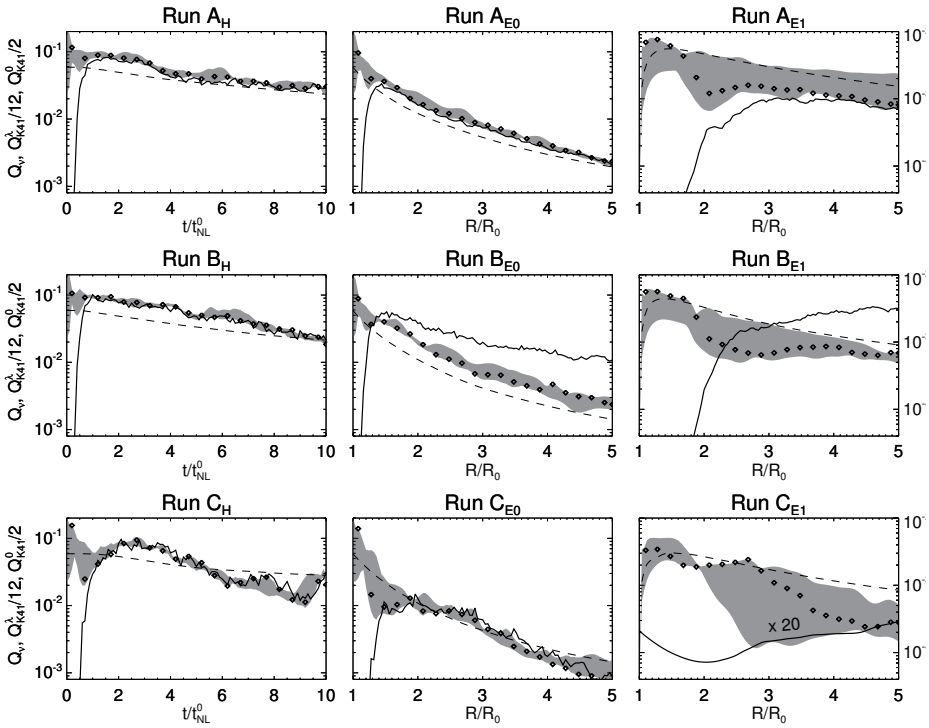

Figure 4. Heating as a function of time (for homogeneous runs, *left column*) or distance (for expanding runs with $\sigma_c = 0,\ 1$, *central* and *right columns*, respectively), for runs listed in Table. 1. From *top* to *bottom*: decreasing turbulence strength. In each panel, the actual heating rate Q_ν is in *bold*. The normalized large-scale estimate $Q^0_{K41}/2$ is plotted with a *dashed line*. The normalized Taylor-scale estimate $Q^\lambda_{K41}/12$ is plotted with symbols (*diamonds*). The *grey shaded area* represents the inertial range estimate $Q_{K41}/12$ evaluated between $k^\lambda/8$ and $2k^\lambda$. Note the *right column* vertical range is different from other panels, and actual heating in the *bottom right panel* is multiplied by 20.

3.2. Heating rate

In Figure 4 we plot the true heating, Q_ν (bold solid line), and heating estimates for all homogeneous and expanding runs, following the same ordering as in Figure 3. Note that we used a specific vertical range in the third column (expanding runs with $\sigma_c = 1$), and that the true heating, Q_ν, in the bottom right panel is multiplied by a factor 20.

We used different normalizations for the inertial range and large-scale heating estimates: $Q_{K41}/12$ and $Q^0_{K41}/2$, respectively. The normalization of Q_{K41} is chosen as a best fit of the inertial range estimate to the true heating, the second derives from Equation 5. The inertial range estimate ($Q_{K41}/12$) is displayed in several forms: the Taylor scale estimate, $Q^\lambda_{K41}/12$, is plotted with diamonds, while heating estimates, $Q_{K41}/12$,evaluated at wavenumbers between $k_\lambda/8$ and $2k_\lambda$ is displayed by the grey area. Note that the width of the grey area provides a measure of the inaccuracy of the method when the spectra do not have a $-5/3$ slope. The large-scale estimate, $Q^0_{K41}/2$, is plotted with a dashed line.

By comparing the bold line and the symbols (diamonds), one sees that for all runs $Q^{\lambda}_{K41}/12$ is an excellent predictor of the true dissipation, Q_ν, as soon as the cascade is fully developed: this happens at times/distances depending on the initial parameters and never for run C_{E1} (initial cross helicity unity), as expected (recall that the true heating is multiplied by a factor 20 in this panel). Note that the cascade onset is simply defined by the time/distance at which true dissipation reaches its maximum: this occurs at particularly large distances in runs with large cross-helicity (right column), but still the agreement between $Q^{\lambda}_{K41}/12$ and Q_ν is good. Note however that no match is found in the last run C_{E1} (right column, bottom panel), for which the maximum dissipation distance is clearly not reached.

The normalized large-scale estimate, $Q^{0}_{k41}/2$, does also a reasonably good job, with estimates being within a factor 2 to the actual dissipation, Q_ν, for all runs, except again for run C_{E1}, as expected.

4. Multishell simulations of the accelerating region

We now consider multishell simulations in the accelerating region, whose parameters are listed in table 2. The bottom boundary is within the chromosphere, at R_0 =1.005 $R_\odot$. In run A, we inject Alfvénic fluctuations with an amplitude $\delta z^{rms}_{+} = 15\ km\ \mathrm{s}^{-1}$, a correlation time of $T^* = 600\ s$, and with the largest forcing perpendicular scale corresponding to the supergranulation scale ($L^{inj}_{\perp 0} = 34$ Mm, recall that injection is on three consecutive shells). The turbulence strength for the reflected fluctuations is $\chi^{-}_0 = T^*/t^{-}_{NL0} = 1.6 > 1$, and it is also approximately the same for the outward propagating fluctuation, χ^{+}_0, since the strong reflection in the whole chromosphere and at the transition region causes $\delta z^{rms}_{-} \lesssim \delta z^{rms}_{+}$ (and as well $\delta u^{rms} \gg \delta b^{rms}$) at the bottom boundary. In runs B, C, and D we increase the strength parameter, χ^{-}_0, by either increasing the correlation time, T_*, doubling the amplitudes, δz^{rms}_{+}, or decreasing the correlation length of the forcing, $L^{inj}_{\perp 0}$, respectively.

4.1. Spectral evolution

Let us first analyze the spectral evolution with height. Figure 5 shows time-averaged energy spectra at increasing distances from the Sun: the top panels show the ρE_+ spectra, the bottom panels show the ρE_- spectra, both compensated by a $k^{-5/3}$ scaling. Spectra at a given position are averaged over about 20 crossing time [2] of the outward propagating fluctuation, $t^{+}_{cross} \sim 5.000$ s, after 20 crossing times are elapsed (i.e. in the interval $t \in [100.000, 200.000]$ s). In each panel, style indicates the altitude: thick solid lines for coronal heights below the maximum of the Alfvén speed, and thin solid lines for heights above $\sim 3\ R_\odot$. The specific positions are $R = [1.03, 1.11, 1.38, 2.73, 4.53, 6.33, 8.13, 9.20]\ R_\odot$, as indicated by arrows in Figure 2a.

[2]Such a long time is necessary to achieve the relaxation of the reflected fluctuations, z_-, that have a much longer crossing time than z_+.

Table 2. Runs for coronal holes: δz_+^{rms} is the rms amplitude of Alfvén waves injected at the surface in 3 consecutive shells, $L_{\perp 0}^{inj}$ is the largest perpendicular scale of the injected waves, and T^* their correlation time. Secondary parameters are the nonlinear time for z_-, $t_{NL0}^- = L_{\perp 0}/(2\pi\delta z_+^{rms})$, and the turbulent strength of z^- at the bottom boundary, $\chi_0^- = T^*/t_{NL0}^-$. Note that the time-averaged rms amplitudes at the bottom boundary are very similar for both species, $\delta z_-^{rms} \lesssim \delta z_+^{rms}$ and so the turbulent strength, $\chi_0^+ = T^*/t_{NL0}^- \simeq \chi_0^-$.

Run	T^* s	δz_+^{rms} km s^{-1}	$L_{\perp 0}^{inj}$ 10^3 km	t_{NL0}^- s	$\chi_0^- \sim \chi_0^+$
A	600	15	34	383	1.6
B	6000	15	34	383	16
C	600	30	34	191	3.1
D	600	15	3.4	38.3	16

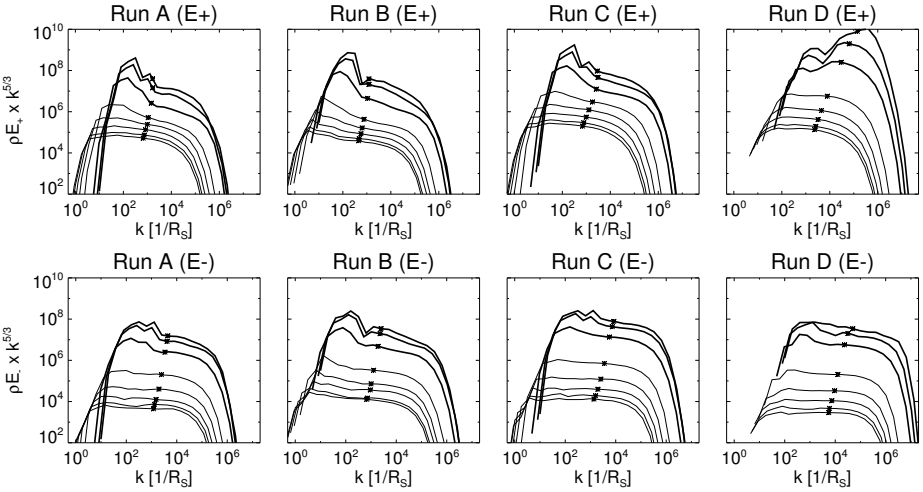

Figure 5. Coronal runs A, B, C, D: energy spectra , compensated by $k^{-5/3}$, $\rho E_+(k)$ (*top panels*) and $\rho E_-(k)$ (*bottom panels*). Crosses: Taylor wavenumber k_λ. The eight spectra shown have decreasing amplitudes at increasing distances from low to high corona (from 1.03 to 10 $R_\odot$, see *arrows* in Figure 2a). *Thick* and *thin lines* correspond respectively to coronal heights below and above the maxima of the Alfvén speed.

Run A is the reference run, with B having a larger correlation time, C a larger wave amplitude, and D a smaller perpendicular scale (see Table 2). All runs show some (complete or not) relaxation towards a $-5/3$ spectral slope, with irregular spectra in the low corona. There (except for run D) excitation is concentrated on very large scales and as the height increases spectra pass progressively from being steep to having a $k^{-5/3}$ scaling. As a rule, the cross helicity (or dominance of the E_+ energy) is concentrated on the largest scales, which explains the slow

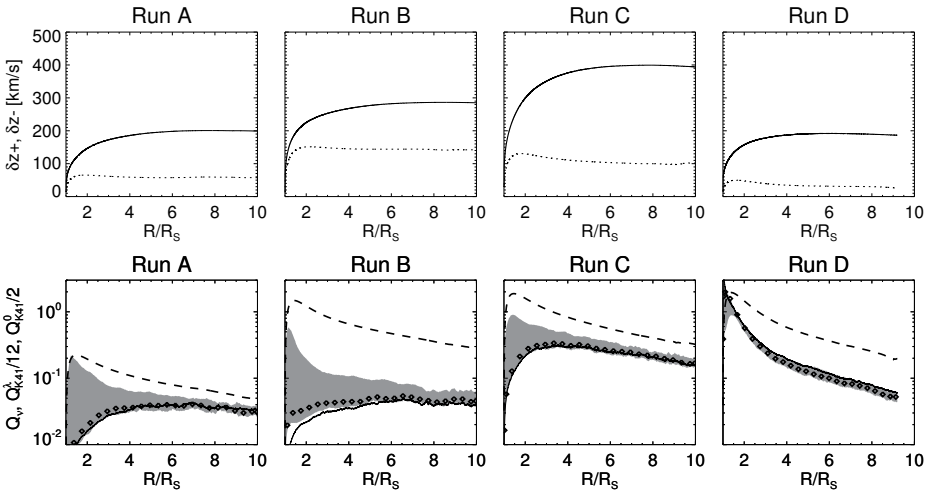

Figure 6. Coronal runs A, B, C, D. *Top panels*: rms amplitudes of the incident (δz_+, *solid lines*) and reflected (δz_-, *dotted lines*) for runs listed in Table. 2. *Bottom panels*: heating vs distance; in each panel, the actual heating rate Q_ν is in *bold*. The inertial-range estimates and large-scale estimates are normalized, see Equation 5, and plotted with symbols (*diamonds*), $Q^\lambda_{K41}/12$, and with a *dashed line*, $Q^0_{K41}/2$, respectively. The *grey shaded area* represents the inertial range estimate $Q_{K41}/12$ evaluated between $k^\lambda/8$ and $2k^\lambda$.

evolution of these scales. A last (expected) property is the larger inertial range of the dominated E_- spectrum, due to the smaller nonlinear time of the z_- field.

Independently of the parameters at injection, we find nice plateaux in the corona layers above 2.7 $R_\odot$, indicating that a scaling close to Kolmogorov holds. The position of the Taylor wavenumber lies in the middle of the plateaux, suggesting that the Taylor scale estimate, Q^λ_{K41}, is a good proxy for the dissipation rate. However, at low-corona heights, the Taylor wavenumber is located in the tails, so we do not expect a good performance of Q^0_{K41} because of the varying slopes at high wavenumbers, if any power-law scaling can be measured.

4.2. Profiles of $z_\pm$

Varying the injection parameters modifies in a clear way the rms amplitudes of the Elsasser fields. In the top panels of Figure 6 we plot the time-averaged rms amplitudes, $\delta z_\pm$, as a function of distance (solid lines for incident waves, and dotted lines for reflected waves). We compare in turn runs B, C, D with run A. Run B has a correlation time ten times larger than run A: as a result, z_+ is increased by a factor 1.5, and z_- by a factor 3. Run C has the incident amplitude twice as large as that of run A, which approximately leads to the same factor 2 for the profiles of both z_+ and z_- in the corona. Run D has the surface perpendicular scale ten times smaller than that of run A: this leads to an almost unchanged z_+ coronal amplitude, but to a smaller z_- amplitude. Note that only A and D have reasonable coronal amplitudes of z_+ (i.e., smaller than 400 km/s).

4.3. Heating

The true heating is shown in the bottom panels of Figure 6 with thick solid lines. The large-scale estimate, $Q^0_{K41}/2$, is shown with a dashed line, the inertial-range estimate at Taylor scale, $Q^\lambda_{K41}/12$, with diamonds, and the gray area is the inertial range estimate at wavenumbers between $k_\lambda/8$ and $2k_\lambda$.

The four runs have large-scale heating curves, $Q^0_{k41}/2$, of similar functional forms, with runs B, C, D showing larger levels than run A by a factor close to 10. This is indeed what is expected when increasing the correlation time, the incident amplitude, and decreasing the perpendicular scale.

In contrast, when examining the true heating rate, the correlation with the boundary conditions parameters is weak. For instance, runs A and B have quasi-identical heating curves: heating is insensitive to the correlation time, although the wave amplitudes are. The Taylor estimate, $Q^\lambda_{K41}/12$, is a remarkable predictor of the true heating, even in the low corona, although the dispersion of the inertial range estimate in the interval $[k^\lambda/8, 2k^\lambda]$ is large there, especially in runs A-C.

The large-scale estimate of the heating appears to be a poor method in the present case of the accelerating region: it is clear that no constant normalization can be found, thus invalidating the use of such an estimate in the accelerating region and, more generally, in a turbulence driven solar wind model.

This is partially in contrast with the cases in the previous section. Indeed, we showed that a simple normalization could be found to provide a good large-scale predictor in the two series: homogeneous and expanding turbulence with zero cross-helicity. However, the third series, expanding turbulence with initial cross-helicity equal to one, led to large-scale heating estimate in excess of the the true heating, as here.

So we conclude that the large cross helicity found in the set of simulations A,B,C,D (Figure 6, top panels) probably explains the difficulty in using the large-scale heating estimate based on rms amplitudes. Indeed, rms amplitudes are heavily based on the large-scale part of the turbulent spectrum. Coming back to the spectral evolution shown in Figure 5, we see that the cross-helicity (or, equivalently, the dominance of the E_+ spectrum) is largest at the large scales, so imposing for them a particularly slow relaxation. It is clear that in these conditions a heating estimate based on rms (or large scale) wave amplitudes will not be appropriate.

5. Conclusion

Let us summarize our results. First consider the inertial range estimate of heating. The measurements of the ratio Q^λ_{K41}/Q_ν in multishell simulations, either of homogeneous turbulence or of expanding wind turbulence, all give remarkably stable results with a ratio 12, close to the value 10 obtained recently via direct 3D MHD simulations in the expanding wind, in the range [0.2, 1] AU (Montagud-Camps, Grappin, and Verdini, 2018). This holds for all the parameters studied,

except for the case of weak turbulence with large initial cross helicity and expansion. As mentioned in the introduction, the ratio $Q^{\lambda}_{K41}/Q \sim 10$ has also been found for slow/cold winds at 1 AU in which the spectral slope is $-5/3$, with Q being estimated with an empirical relation (Vasquez *et al.*, 2007).

The good agreement between multishell results and other independent measurements gives confidence in the predictions of the multishell model in other cases, as that of the wind acceleration range considered in this paper, where no direct measurements of heating are available. In the latter region, we found that the multishell result is again $Q^{\lambda}_{K41}/Q_{\nu} \simeq 12$.

Now consider our main aim, namely the evaluation of the large-scale heating estimate, Q^{0}_{K41}, used in incompressible turbulence driven solar wind models. In this case, the results (i.e., those in the coronal hole case reported in section 4) are much less favorable than those for the inertial range estimate for several reasons.

First, *convergence with increasing heliocentric distance* of Q^{0}_{K41}/Q_{ν} to an asymptotic value is very slow, except for one of the four cases (run C) considered, so it is clear that fixing the ratio to a constant would lead to a poor representation of heating. Second, the *asymptotic value* of Q^{0}_{K41}/Q_{ν} depends strongly on the boundary parameters (correlation time, amplitude, perpendicular scale): Figure 6 shows that the asymptotic ratio $Q^{0}_{K41}/2$ to Q_{ν} varies from 2 to 10, thus the ratio Q^{0}_{K41}/Q_{ν} varies from 4 to 20. Last, such a range of values (from 4 to 20) shows that the large-scale heating formula used systematically in the incompressible turbulence driven solar wind models is largely *overestimated*. Such a flaw further weakens turbulence-driven models that already require elevated values at the boundary conditions (amplitudes and correlation time) to obtain realistic solar winds profiles.

Our conclusion is thus that accelerating the solar wind via incompressible turbulence is more difficult than generally thought, as already pointed out by (van Ballegooijen and Asgari-Targhi, 2016, 2017).

Recently, it has been found that combining compressible and incompressible turbulence (the latter being modeled by a large scale Kolmogorov-like term as Q^{0}_{K41} with an efficiency $c_d = 0.1$) much increases the incompressible heating (Shoda, Yokoyama, and Suzuki, 2018). This is due to the increased amplitude of reflected waves that is caused by density fluctuations (van Ballegooijen and Asgari-Targhi, 2017) and parametric decay (Del Zanna *et al.*, 2015; Shoda and Yokoyama, 2016; Shoda, Yokoyama, and Suzuki, 2018). However, the present results indicate that the large-scale estimate is far from being a robust measure of heating, while the Taylor scale (or more generally an inertial range) estimate is by far preferable.

An interesting way to progress would be to use a compressible 1D solar wind model as Shoda, Yokoyama, and Suzuki (2018), but replacing the large-scale Kolmogorov-like heating term, Q^{0}_{K41}, by a more detailed description of the perpendicular cascade as done here via the multishell model.

Acknowledgments This work has been supported by Programme National Soleil-Terre (PNST/INSU/CNRS). The authors declare they have no conflicts of interest.

References

Beresnyak, A.: 2012, Basic properties of magnetohydrodynamic turbulence in the inertial range. *Mon. Not. Roy. Astron. Soc.* **422**, 3495. DOI. ADS. [Bere_2012]

Bruno, R., Carbone, V.: 2013, The solar wind as a turbulence laboratory. *Living Reviews in Solar Physics* **10**, 2. DOI. [Bruno_Carbone_2013]

Buchlin, E., Velli, M.: 2007, Shell Models of RMHD Turbulence and the Heating of Solar Coronal Loops. *Astrophys. J.* **662**, 701. DOI. ADS. [Buchlin_Velli_2007]

Chandran, B.D.G., Dennis, T.J., Quataert, E., Bale, S.D.: 2011, Incorporating Kinetic Physics into a Two-fluid Solar-wind Model with Temperature Anisotropy and Low-frequency Alfvén-wave Turbulence. *Astrophys. J.* **743**, 197. DOI. ADS. [Chandran_al_2011]

Cranmer, S.R., van Ballegooijen, A.A., Edgar, R.J.: 2007, Self-consistent Coronal Heating and Solar Wind Acceleration from Anisotropic Magnetohydrodynamic Turbulence. *Astrophys. J. Supp. Series* **171**, 520. DOI. ADS. [Cranmer_al_2007]

Del Zanna, L., Matteini, L., Landi, S., Verdini, A., Velli, M.: 2015, Parametric decay of parallel and oblique Alfvén waves in the expanding solar wind. *Journal of Plasma Physics* **81**(1), 325810102. DOI. ADS. [DelZanna_al_2015]

Dmitruk, P., Milano, L.J., Matthaeus, W.H.: 2001, Wave-driven Turbulent Coronal Heating in Open Field Line Regions: Nonlinear Phenomenological Model. *Astrophys. J.* **548**, 482. DOI. ADS. [Dmitruck_al_2001]

Dmitruk, P., Matthaeus, W.H., Milano, L.J., Oughton, S., Zank, G.P., Mullan, D.J.: 2002, Coronal Heating Distribution Due to Low-Frequency, Wave-driven Turbulence. *Astrophys. J.* **575**, 571. DOI. ADS. [Dmitruck_al_2002]

Dong, Y., Verdini, A., Grappin, R.: 2014, Evolution of turbulence in the expanding solar wind, a numerical study. *The Astrophysical Journal* **793**(2), 118. [Dong:2014fi]

Giuliani, P., Carbone, V.: 1998, A note on shell models for MHD turbulence. *EPL (Europhysics Letters)* **43**, 527. DOI. ADS. [Giuliani_Carbone_1998]

Gledzer, E.B.: 1973, System of hydrodynamic type admitting two quadratic integrals of motion. *Soviet Physics Doklady* **18**, 216. ADS. [Gledzer_1973]

Grappin, R., Velli, M., Mangeney, A.: 1993, Nonlinear wave evolution in the expanding solar wind. *Physical Review Letters* **70**(1), 2190. [1993PhRvL..70.2190G]

Hossain, M., Gray, P.C., Pontius, D.H.J., Matthaeus, W.H., Oughton, S.: 1995, Phenomenology for the decay of energy-containing eddies in homogeneous MHD turbulence. *Physics of Fluids* **7**(1), 2886. [1995PhFl....7.2886H]

Lionello, R., Velli, M., Downs, C., Linker, J.A., Mikić, Z., Verdini, A.: 2014, Validating a time-dependent turbulence-driven model of the solar wind. *The Astrophysical Journal* **784**(2), 120. [Lionello:2014db]

Matsumoto, T., Suzuki, T.K.: 2012, Connecting the Sun and the Solar Wind: The First 2.5-dimensional Self-consistent MHD Simulation under the Alfvén Wave Scenario. *Astrophys. J.* **749**, 8. DOI. ADS. [Matsumoto_Suzuki_2012]

Matthaeus, W.H., Minnie, J., Breech, B., Parhi, S., Bieber, J., Oughton, S.: 2004, Transport of cross helicity and radial evolution of Alfvénicity in the solar wind. *Geophysical Research Letters* **31**(1), L12803. [2004GeoRL..3112803M]

Montagud-Camps, V., Grappin, R., Verdini, A.: 2018, Turbulent Heating between 0.2 and 1 au: A Numerical Study. *The Astrophysical Journal* **853**(2), 0. [MontagudCamps:2018ki]

Nigro, G., Malara, F., Carbone, V., Veltri, P.: 2004, Nanoflares and MHD Turbulence in Coronal Loops: A Hybrid Shell Model. *Physical Review Letters* **92**(19), 194501. DOI. ADS. [Nigro_al_2004]

Perez, J.C., Chandran, B.D.G.: 2013, Direct numerical simulations of reflection-driven, reduced magnetohydrodynamic turbulence from the sun to the alfvén critical point. *The Astrophysical Journal* **776**(2), 124. [Perez:2013fb]

Politano, H., Pouquet, A.G.: 1998, von Kármán-Howarth equation for magnetohydrodynamics and its consequences on third-order longitudinal structure and correlation functions. *Physical Review E (Statistical Physics* **57**(1), 21. [1998PhRvE..57...21P]

Shoda, M., Yokoyama, T.: 2016, Nonlinear Reflection Process of Linearly Polarized, Broadband Alfvén Waves in the Fast Solar Wind. *Astrophys. J.* **820**, 123. DOI. ADS. [Shoda_Yokoyama_2016]

Shoda, M., Yokoyama, T., Suzuki, T.K.: 2018, A Self-consistent Model of the Coronal Heating and Solar Wind Acceleration Including Compressible and Incompressible Heating Processes. *The Astrophysical Journal* **853**(2), 0. [Shoda:2018dq]

Shoda, M., Yokoyama, T., Suzuki, T.K.: 2018, Frequency-dependent Alfvén-wave Propagation in the Solar Wind: Onset and Suppression of Parametric Decay Instability. *Astrophys. J.* **860**, 17. DOI. ADS. [Shoda_al_2018b]

Stawarz, J.E., Smith, C.W., Vasquez, B.J., Forman, M.A., MacBride, B.T.: 2009, The Turbulent Cascade and Proton Heating in the Solar Wind at 1 AU. *Astrophys. J.* **697**, 1119. DOI. ADS. [Stawarz_al_2009]

Suzuki, T.K., Inutsuka, S.-i.: 2005, Making the Corona and the Fast Solar Wind: A Self-consistent Simulation for the Low-Frequency Alfvén Waves from the Photosphere to 0.3 AU. *The Astrophysical Journal* **632**(1), L49. [2005ApJ...632L..49S]

Suzuki, T.K., Inutsuka, S.-I.: 2006, Solar winds driven by nonlinear low-frequency Alfvén waves from the photosphere: Parametric study for fast/slow winds and disappearance of solar winds. *Journal of Geophysical Research (Space Physics)* **111**, A06101. DOI. ADS. [Suzuki_Inutsuka_2006]

Tenerani, A., Velli, M.: 2017, Evolving Waves and Turbulence in the Outer Corona and Inner Heliosphere: The Accelerating Expanding Box. *Astrophys. J.* **843**, 26. DOI. ADS. [Tenerani_Velli_2017]

Usmanov, A.V., Goldstein, M.L., Matthaeus, W.H.: 2014, Three-fluid, Three-dimensional Magnetohydrodynamic Solar Wind Model with Eddy Viscosity and Turbulent Resistivity. *Astrophys. J.* **788**, 43. DOI. ADS. [Usmanov_al_2014]

van Ballegooijen, A.A., Asgari-Targhi, M.: 2016, Heating and Acceleration of the Fast Solar Wind by Alfvén Wave Turbulence. *Astrophys. J.* **821**, 106. DOI. ADS. [VB_AT_2016]

van Ballegooijen, A.A., Asgari-Targhi, M.: 2017, Direct and Inverse Cascades in the Acceleration Region of the Fast Solar Wind. *Astrophys. J.* **835**, 10. DOI. ADS. [VB_AT_2017]

van der Holst, B., Sokolov, I.V., Meng, X., Jin, M., Manchester, W.B. IV, Tóth, G., Gombosi, T.I.: 2014, Alfvén Wave Solar Model (AWSoM): Coronal Heating. *Astrophys. J.* **782**, 81. DOI. ADS. [VanDerHolst_al_2014]

Vasquez, B.J., Smith, C.W., Hamilton, K., MacBride, B.T., Leamon, R.J.: 2007, Evaluation of the turbulent energy cascade rates from the upper inertial range in the solar wind at 1 AU. *J. Geophys. Res.* **112**(A7), A07101. [2007JGRA..11207101V]

Verdini, A., Grappin, R.: 2012, Transition from Weak to Strong Cascade in MHD Turbulence. *Physical Review Letters* **109**(2), 025004. DOI. ADS. [Verdini_Grappin_2012]

Verdini, A., Velli, M.: 2007, Alfvén Waves and Turbulence in the Solar Atmosphere and Solar Wind. *Astrophys. J.* **662**, 669. DOI. ADS. [Verdini_Velli_2007]

Verdini, A., Grappin, R., Velli, M.: 2012, Coronal heating in coupled photosphere-chromosphere-coronal systems: turbulence and leakage. *Astron. Astrophys.* **538**, A70. DOI. ADS. [Verdini_al_2012]

Verdini, A., Velli, M., Buchlin, É.: 2009, Turbulence in the Sub-Alfvénic Solar Wind Driven by Reflection of Low-Frequency Alfvén Waves. *The Astrophysical Journal Letters* **700**(1), L39. [2009ApJ...700L..39V]

Verdini, A., Velli, M., Matthaeus, W.H., Oughton, S., Dmitruk, P.: 2010, A Turbulence-Driven Model for Heating and Acceleration of the Fast Wind in Coronal Holes. *Astrophys. J. Lett.* **708**, L116. DOI. ADS. [Verdini_al_2010]

Verdini, A., Grappin, R., Pinto, R.F., Velli, M.: 2012, On the Origin of the 1/f Spectrum in the Solar Wind Magnetic Field. *The Astrophysical Journal Letters* **750**(2), L33. [2012ApJ...750L..33V]

Verdini, A., Grappin, R., Hellinger, P., Landi, S., Müller, W.-C.: 2015, Anisotropy of Third-order Structure Functions in MHD Turbulence. *The Astrophysical Journal* **804**(2), 119. [2015ApJ...804..119V]

Wang, Y.-M.: 1994, Polar plumes and the solar wind. *The Astrophysical Journal* **435**, L153. [Wang:1994bv]

Wang, Y.-M., Grappin, R., Robbrecht, E., Sheeley, N.R. Jr.: 2012, On the Nature of the Solar Wind from Coronal Pseudostreamers. *Astrophys. J.* **749**, 182. DOI. ADS. [Wang_al_2012]

Woolsey, L.N., Cranmer, S.R.: 2015, Time-dependent Turbulent Heating of Open Flux Tubes in the Chromosphere, Corona, and Solar Wind. *Astrophys. J.* **811**, 136. DOI. ADS. [Woolsey_Cranmer_2015]

Yamada, M., Ohkitani, K.: 1987, Lyapunov spectrum of a chaotic model of three-dimensional turbulence. *Journal of the Physical Society of Japan* **56**, 4210. DOI. ADS. [Yamada_Ohkitanu_1987]